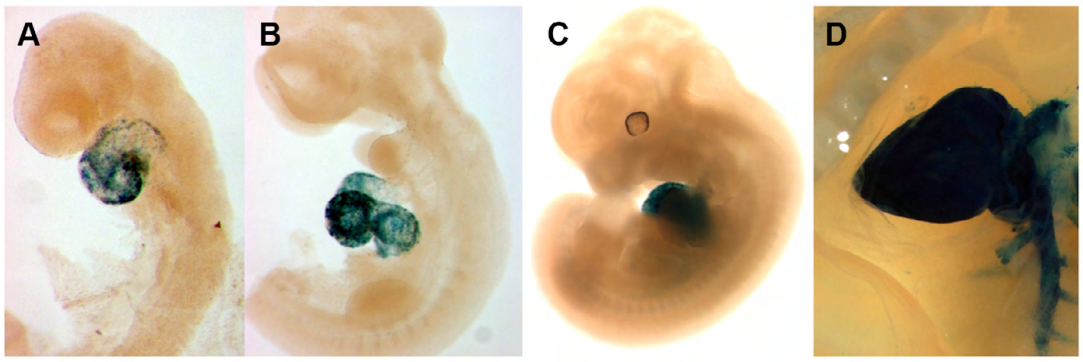

Fig. S1. Analysis of X-Gal-stained E9-E18 embryos from *H1-Ncx-cre; R26R* indicator mice. (**A-D**) *H1-Ncx-cre* transgenic males were bred to *R26R* females. Whole-mount X-Gal-stained embryos were either photographed whole at E9 (A), E9.5 (B) or E12 (C) or partially dissected to expose the heart (D) at E18 to visualize Cre-expressing cells. Note that *lacZ* expression is restricted to the heart (A-C). Fetal hearts (D) continue to exhibit robust Cre activity within the ventricles and atria but now Cre activity is also observed within the smooth muscle cells lining the major lung vasculature.

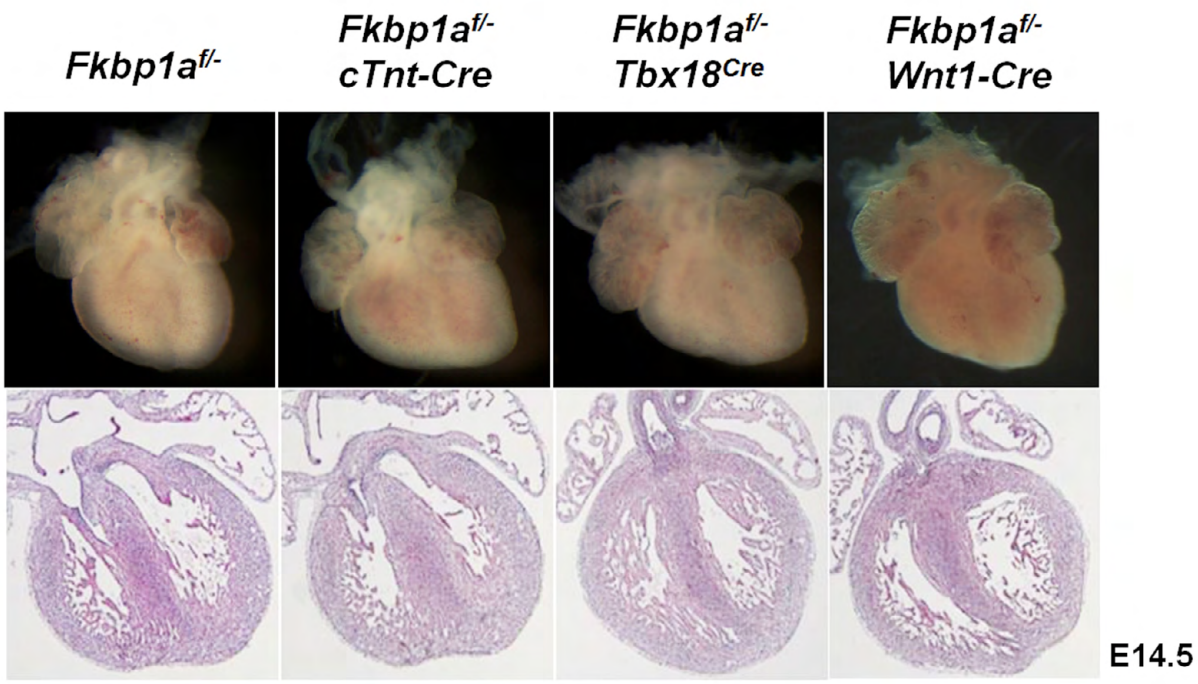

Fig. S2. Normal ventricular wall formation upon myocardial, epicardial and neural crest cell-specific ablation of *Fkbp1a*. *cTnt-cre* mice were used to ablate *Fkbp1a* in early developing myocardium. *Fkbp1a*$^{flox/-}$*:cTnt-cre* mice develop a normal ventricular wall. Several lines of evidence suggest that epicardial-derived signaling can exert effects on ventricular wall growth and formation. As *Nkx2.5*^{cre} deletes *Fkbp1a* from the epicardial lineage, we examined whether Fkbp1a function within the epicardium regulates ventricular wall formation using *Tbx18*^{cre} mice, which have previously been shown to drive Cre mainly to the developing epicardium and, potentially, a small population of cardiomyocytes. Similar to results obtained with cardiomyocyte-specific Cre drivers, *Fkbp1a*$^{flox/-}$*:Tbx18*^{cre} mice exhibit normal development of the ventricular wall and survive to adulthood. Additionally, neural crest cell-restricted ablation of *Fkbp1a* via *Wnt1-cre* mice also did not generate a left ventricular noncompaction phenotype. Combined, these data indicate that cardiomyocyte, epicardial and cardiac neural crest cell populations are not the primary cell types contributing to the ventricular hypertrabeculation and noncompaction phenotypes in *Fkbp1a*-deficient mice.

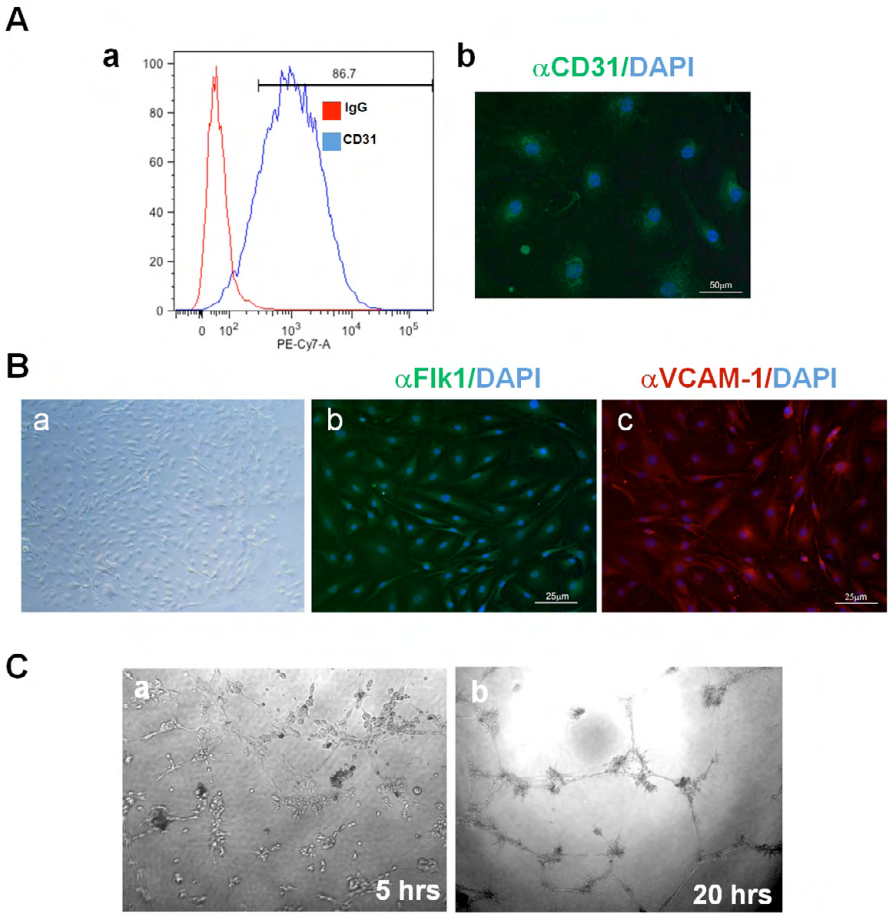

Fig. S3. Characterization of murine endothelial cells isolated from neonatal *Fkbp1a*$^{flox/flox}$ mice. (**A**) Initial isolation and characterization of *Fkbp1a*$^{flox/flox}$ endothelial cells using the endothelial surface marker CD31. (a) Flow cytometry analysis for CD31-positive cells. (b) Immunofluorescent staining using anti-CD31 antibody to confirm flow cytometry data. (**B**) Confirmation of endothelial cell morphology and molecular markers for *Fkbp1a*$^{flox/flox}$ endothelial cells by immunofluorescence staining. (a) Typical endothelial morphology of cells continuously cultured and maintained for 74 days (phase contrast image, ×100). (b,c) Representative immunofluorescence images of *Fkbp1a*$^{flox/flox}$ cells stained with antibodies against the endothelial surface makers Flk1 and Vcam1 (×200). (**C**) MatriGel tube-forming assay confirming the functionality of *Fkbp1a*$^{flox/flox}$ endothelial cells. *Fkbp1a*$^{flox/flox}$ endothelial cells start to form a tube after 5 hours of culture (a) and are able to form well-defined tubular structures within 20 hours (b).

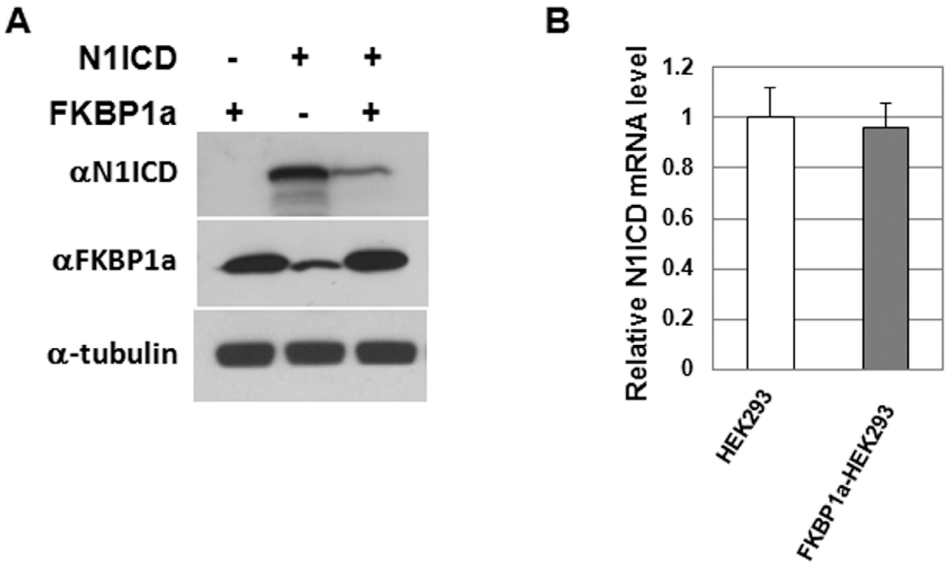

Fig. S4. Analysis of N1ICD level in *FKBP1A*-overexpressing cells. (**A**) Western blot analysis shows that the N1ICD protein level is significantly lower in FKBP1A-HEK293 cells than in HEK293 control cells. (**B**) qRT-PCR analysis shows similar N1ICD mRNA level in FKBP1A-HEK293 and control cells.

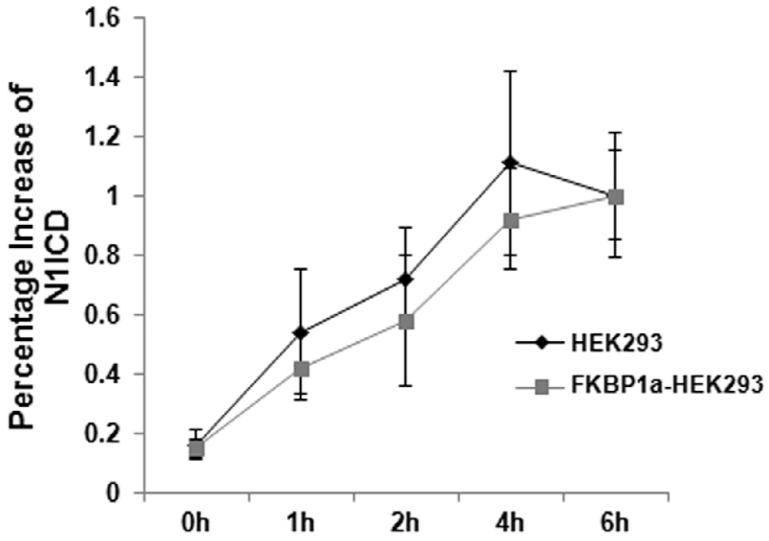

Fig. S5. Assessment of the rate of increase of N1ICD in FKBP1A-HEK293 and HEK293 cells. There is no statistical difference in the rate of increase of N1ICD between FKBP1A-overexpressing FKBP1A-HEK293 and control HEK293 cells.

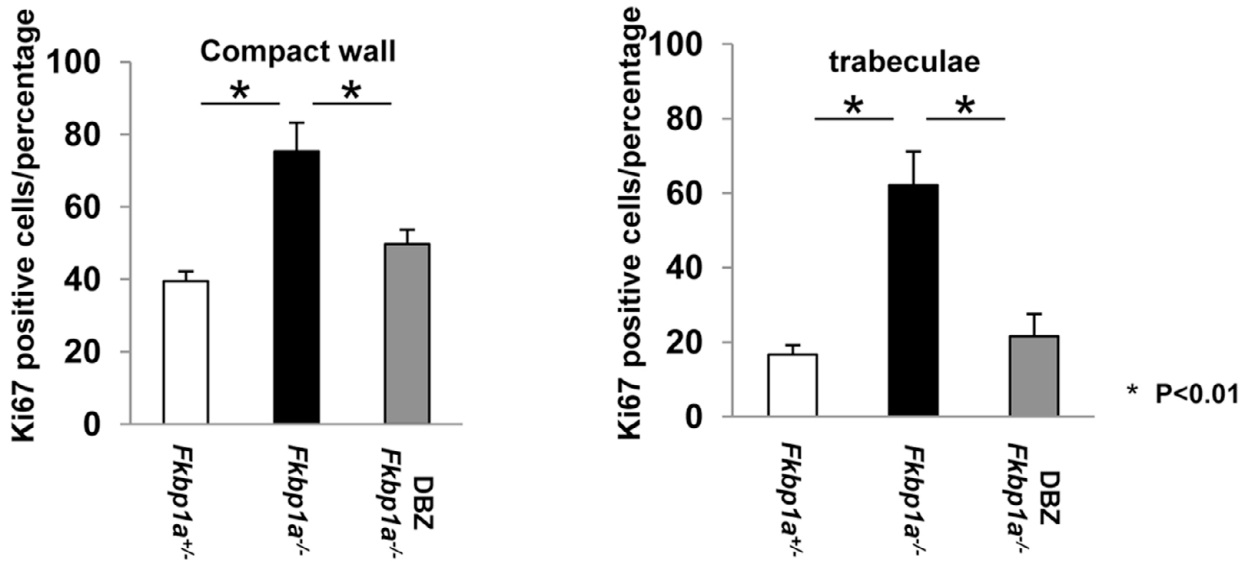

Fig. S6. Quantitative comparison of proliferative activities of DBZ-treated *Fkbp1a* mutant and control hearts. DBZ treatment significantly reduced cellular proliferative activity in both compact wall and trabecular myocardium of *Fkbp1a*-deficient hearts.